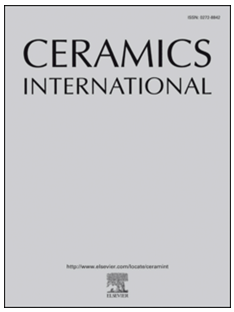


# A facile platform for the synthesis of metal–oxide composites

Agustín Avalos, Eugenia Zelaya, Marcelo R. Esquivel

PII: S0272-8842(20)33362-9

DOI: https://doi.org/10.1016/j.ceramint.2020.11.046

Reference: CERI 26997

To appear in: *Ceramics International*

Received Date: 12 June 2020

Revised Date: 29 October 2020

Accepted Date: 7 November 2020

Please cite this article as: A. Avalos, E. Zelaya, M.R. Esquivel, A facile platform for the synthesis of metal–oxide composites, *Ceramics International*, https://doi.org/10.1016/j.ceramint.2020.11.046.

# A facile platform for the synthesis of metal–oxide composites

Agustín Avalos [a], Eugenia Zelaya [b], Marcelo R. Esquivel [b,c]

[a] Instituto Sabato (UNSAM - CNEA) Av. Gral Paz 1499. San Martín, Buenos Aires, Argentina.

[b] Centro Atómico Bariloche (CNEA-CONICET) – Av. Bustillo km 9.5 – Bariloche – Río Negro – (8400) – Argentina

[c] UNCo- Bariloche. Quintral 1250 – Bariloche (8400) Rio Negro Argentina.

Highlights:

The paper reports the original non-wet synthesis of a metal-oxide composite from metals/alloys as precursors.

The work reports the original experimental value of the enthalpy of formation of the $La_{0.25}Ce_{0.52}Nd_{0.17}Pr_{0.06}O_2$.

The work reports the structural transformation from cubic to hexagonal of the $La_{0.25}Ce_{0.52}Nd_{0.17}Pr_{0.06}$ alloy induced by milling.

The work reports the crystallographic refinement of both the cubic and the hexagonal structures of the $La_{0.25}Ce_{0.52}Nd_{0.17}Pr_{0.06}$ alloy.

Abstract

A versatile platform for the production of metal-oxide composites is reported in this work. A $La_{0.25}Ce_{0.52}Nd_{0.17}Pr_{0.06}O_2$ – 3Ni composite is selected for this study. The composite is fabricated in a two-step method including mechanical milling of the

metals/alloys and thermal treatment in air and $H_2$. The mechanism of synthesis includes the structural transformation from cubic to hexagonal of the polymorphs present in the starting $La_{0.25}Ce_{0.52}Nd_{0.17}Pr_{0.06}$ alloy. The transformation is induced by milling. As a part of the analysis, the enthalpy of formation of the $La_{0.25}Ce_{0.52}Nd_{0.17}Pr_{0.06}O_2$ compound is reported. The work reports a platform for the synthesis of composites. The microstructure of the composites is tunable for the use in in different technological applications.

Key words

Milling [A] , Electron microscopy [B] , $La_{0.25}Ce_{0.52}Nd_{0.17}Pr_{0.06}$ alloy , Chemical properties [C]

## 1. Introduction

The synthesis of metal-oxide composites is a subject of current interest in the ceramic field because of the technological applications of these compounds. These composites are used in both the energy conversion and the catalysis fields [1-2]. These applications require $CeO_2$ based-Ni compounds with the potential to tune the composition, structure and nanostructure [3-4]. Therefore, both reviews and original reports on these composites manufacture methods are currently published [5-6].

The synthesis methods of these composites can be mainly divided in wet and dry methods. The wet methods are mostly associated to the fabrication stages that involve the use of liquids either to synthesize or to favor the fabrication of the

composite including wet-milling. The sol-gel method, autocombustion, hydration method and wet impregnation are among the most representative of them [7-10]. Unlike the wet methods, the dry methods do not involve liquids at any stage of the fabrication of the composite. The dry reactive milling is the most representative of them, although the references are scarce on the subject. Nevertheless, the combination of wet milling along other methods is referenced in Zhang et.al. [12]. Although both fields of synthesis have their advantages, the actual objective is to obtain an appropriate structure for the selected technical application. This statement means that not all reported synthesis methods are convenient for the same goal. For example, if a nanostructured composite is the objective, then wet methods are probably the most appropriate ones [8-11]. This means that a given fabrication method is strongly related to the application. Then, simpler platforms of synthesis which product can be modified to offer tunable nanostructures, microstructures or compositions should be a further step on the fabrication of $CeO_2$ based-Ni composites.

In this work, an original dry fabrication platform for $CeO_2$ based-Ni composites is reported by using an original metal-alloy mixture as precursor. The fabrication method avoids the use of liquids and tunes both the nanostructure and microstructure of the final composites. The platform offers a set of tunable conditions for the synthesis of composites and consists mainly of two steps: milling and heat treatment. After milling, the obtained composite is a nanostructured powder with an intimate metal-oxide contact. After thermal treatment, the obtained

composite is a micro structured pellet. The composite has compounds with crystalline surfaces and well-developed boundaries between the constituents and a final porous structure with a well interconnected matrix of each component. Both products have the potential needed to be used in energy conversion applications.

## 2. Material and methods

### 2.1 Materials

Ar (Linde Gas, 99,999%), $H_2$ (Linde Gas, 99,999%) and synthetic air (Linde Gas) are used in this work. Ni (Sigma/Aldrich 99.99%, -100 Mesh) and chunks of $La_{0.25}Ce_{0.52}Nd_{0.17}Pr_{0.06}$, Reacton, 99,6%) are used as precursors. A nominal composition of 3Ni-$La_{0.25}Ce_{0.52}Nd_{0.17}Pr_{0.06}$ (mole/mole) or (0.55)/(0.45) mass percent is selected for this work. A sample mass of 10 g and stainless steel balls are set in a stainless steel chamber. A ball mass to sample mass ratio of 28 is chosen. The mixture is mechanically milled in a Retsch 100 mill under controlled $Ar/O_2$ atmosphere (5/95% v/v). A milling speed of 200 rpm is selected. The samples are withdrawn from chamber at selected times of milling of 30, 60, 90, 120, 180 and 300 min. The thermal treatments in air are done in a commercial furnace at 1400 °C for 24 h. The thermal treatments under flowing $H_2$/Ar in are done in a laboratory oven-coupled to an ad-hoc designed gas supply system at 800 °C for 8 h. A flow rate of 100 ml/min is used for this task.

### 2.2 Methods

The room temperature X-ray diffraction (XRD) measurements are done in a PANalytical Empyrean diffractometer operated at 40 kV and 30 mA. The X-ray measurements are refined by the Rietveld method [13]. The microstructure parameters, strain and crystallite size, are obtained from the Rietveld measurements using a microstructure model [14]. The scanning electron microscopy (SEM) measurements are done in a FEI Inspect S50 microscope operated at 30 kV – 5kV range. The energy dispersive spectroscopy (EDS) elemental mapping and line-scan measurement are done using a EDAX detector coupled to the microscope. The transmission electron microscopy (TEM) measurements are done in a FEI-TECNAI G20 F2 field emission microscope operated at 200 kV.

The differential scanning calorimetry (DSC) runs are done in a TA Instruments 2910 calorimeter. The measurements are done using an Ar flow of 120 ml/min and stagnant air from room temperature to 570 °C range. The selected mass sample is 20 mg. The sample is enclosed in aluminum hermetic pans. Non isothermal measurements are done at 5 °C/min. The enthalpy measurements are done considering the following relationship:

$$m.\Delta Hf = Q_e \quad (1)$$

where m (mol) is the sample mass, $\Delta H$ (kJ/mol) is the enthalpy of the process considered and $Q_e$ (kJ) is the experimental heat obtained assuming that the system is completely adiabatic [15].

## 3. Discussion and Results

### 3.1. The first step of the platform: The mechanical milling of the metal/alloy constituents

#### 3.1.1 The aggregation state of the starting metal/alloys

The search of a homogenous composition during the fabrication of the desired alloy /composite makes the mechanical alloying process highly dependent of the aggregation state of the starting constituents because the feasibility of the milling process depends on the compositional and structural properties of the compounds involved in the mixture [16]. Then, the microstructural properties of the starting components are studied first.

The figures 1a and 1b show the diffractograms of the $La_{0.25}Ce_{0.52}Nd_{0.17}Pr_{0.06}$ alloy and Ni, respectively. Both samples are refined using the Rietveld method [13-14]. Two structures are found in the diffractogram of Figure 1.a. These structures crystalize in two different systems: cubic ($F\,m\,\bar{3}\,m$) and hexagonal ($P6_3/mmc$). The peaks of Figure 1a are indexed according to these two structures. The structures of the $La_{0.25}Ce_{0.52}Nd_{0.17}Pr_{0.06}$ sample are refined assuming a random distribution of the lanthanide elements in the Wyckoff positions of each polymorph. It is assumed that each polymorph has the same nominal composition. The Table 1 shows the summary of the refinement results.

The hexagonal polymorph is refined as isomorphic to the DHCP or double hexagonal compact phase reported in the literature for pure La, Ce, Nd and Pr [17,18]. The cell parameters of this $P6_3/mmc$ phase are compared to those of the

pure metals in Table 2. As observed for this alloy in Table 2, the basal parameter *a* is the shortest while the *c* parameter is the largest. The volume of the alloy is the second largest compared to the volumes of the pure metals. This result suggests that might be an ordering on the positions of the atoms indicating that positions 2c might be preferentially occupied by La atoms. The successive refinements done to the sample shows no conclusive result.

The cubic polymorph is refined as isomorphic to the FCC (face centered cubic) phase of the pure metals La,Ce,Nd and Pr [18-21]. The cell parameters of the alloy and those of the pure metals are compared in Table 2. The lanthanides atomic radii are 2.74 Å (La), 2.70 Å (Ce), 2.64 Å (Nd) and 2.67 Å(Pr) [ 22]

As observed, the *a* parameter of the La ($F\,m\,\bar{3}\,m$ ) is the largest and that of the Nd ($F\,m\,\bar{3}\,m$) is the smallest [12-14]. It is coincident with the size of the atom radii of these metals enumerated previously. Then, the result obtained is reasonable because the atomic La content is 0.25% and the $La_{0.25}Ce_{0.52}Nd_{0.17}Pr_{0.06}$ alloy has the second largest *a* parameter. The cubic polymorph is refined with a random distribution of the lanthanide atoms according to the nominal composition.

For the La, Ce, Nd and Pr or their binary alloys, the DHCP structure is the one stable at room temperature and room pressure [21, 23-26]. The $F\,m\,\bar{3}\,m$ phase is not stable at room temperature for the pure lanthanides or the respective binary alloys [23-26]. To the best of our knowledge, there is no references studying the stability of the phases for quaternary alloys such as the $La_{0.25}Ce_{0.52}Nd_{0.17}Pr_{0.06}$ alloy. The Rietveld refinement shows that the mass percent of the $F\,m\,\bar{3}\,m$ phase

is 95% and that of $P6_3/mmc$ is 5% as seen on Table 1. If the quaternary alloy verifies the tendency of the binary alloys, the $Fm\bar{3}m$) phase should not occur at room temperature and pressure. Nevertheless, this alloy does not correspond to a sample obtained in equilibrium. The $La_{0.25}Ce_{0.52}Nd_{0.17}Pr_{0.06}$ is a commercial sample obtained from electrodes that come from an electro-reduction process [27]. These electro-reduction methods are quickly achieved at non-equilibrium conditions [27]. Then, the short time and temperatures higher than room temperature do not favor the formation of the DHCP phase. Therefore, the presence of the cubic polymorph at room temperature and pressure are due to the kinetics of the synthesis process of the $La_{0.25}Ce_{0.52}Nd_{0.17}Pr_{0.06}$ alloy that inhibits the formation of the double hexagonal phase. Neither the cubic nor the hexagonal structure informed here for this alloy composition is currently reported in the literature to the best of the knowledge of the authors.

The profile of the diffractogram of Figure 1.a shows structures with a low degree of crystallization. This feature is quantified by calculating the crystallite size (*D*) and strain (*s*). These parameters are calculated by using the Rietveld method. The summary of the microstructural parameters is presented in Table 2 for the selected peaks of each phase. The selected peaks are either the most intense or isolated without shoulders. As observed, the values of *D* are lower than 200 Å or 20 nn for all selected peaks. It indicates that the polymorphs have low crystalline degree. This feature is also due to the fast kinetics of the electro reduction process that does not allow the growth in equilibrium of the crystalline domains.

The Figure 1b shows the diffractogram of the starting Ni. The Ni structure is more crystalline than those of the polymorphs of Figure 1a. The summary of the Rietveld refinement is summarized in Table 1. The structural parameters are similar to those referenced in the literature [28]. The Ni peaks have a good peak-to-background ratio indicating a crystalline structure. The summary of the microstructural properties is shown in Table 3. The *D* values of Ni are higher than the values of the polymorphs of the $La_{0.25}Ce_{0.52}Nd_{0.17}Pr_{0.06}$ alloy . These polymorphs are strained structures as deduced from the strain values of Table 3. Unlike these structures, the Ni one has strain values near to zero. As seen later, the starting microstructural characteristics of the both $La_{0.25}Ce_{0.52}Nd_{0.17}Pr_{0.06}$ and Ni affects the milling process.

3.1.2. The milling of the system

The Figure 2 shows the diffractograms of the $La_{0.25}Ce_{0.52}Nd_{0.17}Pr_{0.06}$ - 3Ni mixture milled in $Ar/O_2$ atmosphere. The diffractograms correspond to the samples milled for 30, 90, 120, 180 and 300 min. The Figure 3 shows a detail of the diffractograms for the same samples in the 25- 35 degrees range. All the diffractograms are refined by the Rietveld method. The Figures 4a, 4b and 4c show a detail of the mass% of the phases , the crystallite size (D) and strain (s) as a function of the milling time. The evolution of the mechanical alloying is described as follows:

At 0 min, the mixture is added to the mill as indicated in the nominal composition. No milling is done. Therefore, the starting composition is 45 %Ni and 55% $La_{0.25}Ce_{0.52}Nd_{0.17}Pr_{0.06}$ as shown in Figure 4a . The values of *D* and *s* are indicated in Table 3 and Figure 4.b and Figure 4c.

At 30 min, the detected phases are Ni and the polymorphs of the $La_{0.25}Ce_{0.52}Nd_{0.17}Pr_{0.06}$ alloy as shown in the Figure 2a and the diffractogram 3a. .Although the alloy has low crystallinity, it is possible to observe both polymorphs as shown in the diffractogram of the Figure 3a. The relative height of the peaks of the hexagonal phase increases as the peaks of the cubic one decrease with respect to the starting alloy. It indicates that the milling process destabilizes the cubic phase inducing the transformation to the more stable hexagonal phase. These two structures are barely detected in the diffractogram at 30 min due to their low crystallinity with values near 40 Å as presented in Table 2 and Figure 4.c. Their combined mass sample percent is less than 5% despite the fact that the starting nominal mass is 56%. Then, the Rietveld refinements of Figure 4a only considers the crystalline phases with D sizes larger than 40 Å. Unlike the peaks of $La_{0.25}Ce_{0.52}Nd_{0.17}Pr_{0.06}$ , the peaks of Ni are clearly observed in Figure 2a due to their large *D* values and low *s* values as quantified for {111} in Figures 4b and 4c. That is why these dominant phases are the only ones that appear in Figure 4 a, Figure 4b and Figure 4c.

At milling times of 60 min, the main crystalline phase is still Ni. The {111}, {200} and {220} diffraction peaks are clearly observed in Figure 2b. The Ni mass% is

increased in Figure 4a owing to the fact that this phase is the most crystalline of all phases detected. The *D* diminishes and the *s* rises as milling progresses as shown in Figures 4b and 4c, respectively. At this milling time, the XRD technique detects the $La_{0.25}Ce_{0.52}Nd_{0.17}Pr_{0.06}O_2$ phase. The oxide is formed due to the reaction with the oxygen of the $O_2$/Ar mixture. As the oxide nucleates, the {111 peak} of $La_{0.25}Ce_{0.52}Nd_{0.17}Pr_{0.06}O_2$ appears as indicated in Figure 3b. The oxide is a more strained phase than Ni as observed in Figures 4b and 4c. The $La_{0.25}Ce_{0.52}Nd_{0.17}Pr_{0.06}O_2$ presents a *D* value smaller than Ni. The oxide presents an *s* value one order of magnitude higher than that of Ni. The two phases of the $La_{0.25}Ce_{0.52}Nd_{0.17}Pr_{0.06}$ alloy are still observed as shown in Figure 2b. The {100} and {101} peaks of the hexagonal phase and the {111} peak of the cubic phase are still observed at this milling time. But the milling process decreases their crystallinity with respect to the milling time of 30 min.

At 90 min, Ni is the most crystalline phase and Ni has the higher mass % as observed in Figure 4a. The peaks are clear and well defined as seen in Figure 2c. The microstructural parameters are quantified in Figures 4b and 4c. The milling process affects slightly the phase and both *D* and *s* reach a plateau. The milling process affects both the hexagonal and cubic phase of the $La_{0.25}Ce_{0.52}Nd_{0.17}Pr_{0.06}$ alloy and destabilizes the last one. At this milling time, the $La_{0.25}Ce_{0.52}Nd_{0.17}Pr_{0.06}O_2$ increases its mass % on the mixture up to 18% as presented in Figure 4a. The {111} peak of the oxide evolves along to the {100} and {101} peaks of the $La_{0.25}Ce_{0.52}Nd_{0.17}Pr_{0.06}$ alloy . The oxide forms as a strained structure as shown in

Figure 4c with small crystallite sizes as seen in Figure 4b. It is because the oxide nucleates on the small crystallite sizes of the alloy while being milled. As a result, the growth of the crystalline domains is limited by the kinetics of the nucleation-and-growth of the oxide and the fracture process of the crystalline domains due to the milling.

From 120 min to 300 min, the fracture-cold welding cycle of the milling process affects slightly the main crystalline phases: Ni and $La_{0.25}Ce_{0.52}Nd_{0.17}Pr_{0.06}O_{2.}$ As observed in Figures 2 d to 2 f, the Ni peaks do not show strong changes. The Ni phase reaches a plateau in mass % value close to 61% of the mixture at 300 min as shown in Figure 4a. The microstructural parameters of Ni do not change strongly in this period of milling. Both *D* and *s* reach a plateau in their respective curves as observed in Figures 4b and 4c. The final values of *D* an *s* are 480 Å and 0.18%, respectively. In this milling period, the $La_{0.25}Ce_{0.52}Nd_{0.17}Pr_{0.06}O_2$ evolves up to a mass % of 38 % at 300 min as observed in Figure 4a. The {111} and {200} peaks of this phase evolve as the milling process progresses. The change due to milling is observed in Figures 2d to 2f and diffractograms d to f of Figure 3. The phase reaches a *D* value near 145 Å at 300 min as shown in Figure 4b. The phase has an *s* value near 1% at 300 min as shown in Figure 4c. The milling processing of the $La_{0.25}Ce_{0.52}Nd_{0.17}Pr_{0.06}$ - 3Ni in $O_2$/Ar for 300 min leads to the formation of a $La_{0.25}Ce_{0.52}Nd_{0.17}Pr_{0.06}O_2$ - 3Ni composite. The final oxide has an *s* value close to 1% and *D* values near to 145 Å. Despite the 300 min of milling, the resulting Ni is a relaxed structure with *s* values close to 0.18% and with a crystallite size value *D*

near to 500 Å. The key of this treatment is the addition of the $O_2$ to the process. The oxygen reacts preferentially with the $La_{0.25}Ce_{0.52}Nd_{0.17}Pr_{0.06}$ alloy. The global reaction during the milling of the composite occurs according to equation 2:

$$La_{0.25}Ce_{0.52}Nd_{0.17}Pr_{0.06} + O_2 = La_{0.25}Ce_{0.52}Nd_{0.17}Pr_{0.06}O_2 \; ; \; \Delta H° = - 890 \pm 1 \; kJ.mol^{-1} \quad (2)$$

The reaction (2) is highly exothermic. To quantify the enthalpy of formation of the oxide, we measure the reaction by differential scanning calorimetry. The measurement is shown in Figure 5. It is done in stagnant air at $5°C.min^{-1}$ and the deviation to negative values is assigned to exothermic events. The experimental curve is shown in continuous black line and the baseline in dotted black line. As temperature rises, the curve deviates from the baseline indicating the starting temperature of reaction at 70 ± 1 °C. The reaction progresses slowly up to 200 °C forming a shoulder of the main peak. At temperatures higher than 200 °C, the reaction accelerates up to the maximum of the curve, the peak, at 302 ± 1 °C. After that, the curve returns to the baseline reaching the end of the reaction at 355 ± 1 °C. The slight asymmetry of the main peak and the presence of a shoulder to the left indicates that the reaction progresses in, at least, two consecutive steps. The obtained value of $\Delta H°$ is equal to - 890 ± 1 $kJ.mol^{-1}$. This enthalpy value is an original result of this work and it is not reported elsewhere to the best of our knowledge. The heat of formation value is slightly smaller than the corresponding

values of enthalpy of formation of $CeO_2$ and $PrO_2$, the only two lanthanide elements of the alloy that forms an stable dioxide [29-30]. The reported values for $CeO_2$ and $PrO_2$ are - 1090.4 ± 1.0 kJ/mol and - 959.8 ± 4.1 kJ/mol, respectively [29-30]. Then, the found value for the enthalpy of formation of the $La_{0.25}Ce_{0.52}Nd_{0.17}Pr_{0.06}O_2$ is reasonable because the oxide should be less stable than $CeO_2$ and $PrO_2$ owing to the fact that the $La_{0.25}Ce_{0.52}Nd_{0.17}Pr_{0.06}O_2$ incorporates trivalent $La^{+3}$ and $Nd^{+3}$ elements to the fluorite-type structure of this oxide.

The milling process shows no formation of NiO and no formation of intermetallics between $La_{0.25}Ce_{0.52}Nd_{0.17}Pr_{0.}06$ and Ni. The formation of the $La_{0.25}Ce_{0.52}Nd_{0.17}Pr_{0.06}O_2$ at short milling times avoids the alloying of the starting constituents. There is also no elemental substitution in the structures of either Ni or the $La_{0.25}Ce_{0.52}Nd_{0.17}Pr_{0.}0_6$ or in the oxide. This assessment is verified by comparing the cell parameters of Ni and $La_{0.25}Ce_{0.52}Nd_{0.17}Pr_{0.06}O_2$. The *a*-cell parameter value of Ni changes from 3.5283(6) at 0 min to 3.5217(3) at 300 min. while the *a* value of the oxide changes from 5.5379(0) at 60 min to 5.5237(0) at 300 min. Both changes in the corresponding *a*-cell parameters values are negligible. Therefore, neither the elemental substitution occurs within either of these structures nor the extension of the solubility range of the Ni occurs in either the rich or poor side of the binary $La_{0.25}Ce_{0.52}Nd_{0.17}Pr_{0.}06$ –Ni phase diagram [16]. This last assessment is in agreement with the behavior observed in all of the binary phase diagrams of the La-Ni, Ce-Ni, Pr-Ni and Nd-Ni systems [23-26].

Although highly statistical, the traditional X-ray diffraction technique has limitations to properly detect crystalline domains smaller than 100 Å. Therefore, we use the TEM technique to characterize crystalline domains with sizes smaller than this value.

The Figure 6 shows TEM measurements on a $La_{0.25}Ce_{0.52}Nd_{0.17}Pr_{0.}0_6$ $O_2$ particle identified in the sample milled in $O_2$/Ar for 300 min. The Figure 6a shows a selected area diffraction (SAED) ring pattern. The diffracted spots that form rings fit to an *F m* $\bar{3}$ *m* structure. The material is polycrystalline and presents crystalline ordering. The calculated parameter is 5.5 ±0.5 Å. Within the resolution of the technique, this value is close to the value shown in Table 4 for this structure. The Figures 6b and 6c show the bright field and dark field of the particle which SAED is shown in 6a. The bright field micrograph shows particles distributed in agglomerates with sizes bigger than 300 nm x 300 nm. The dark field image shows a crystallite size distribution between 15 and 20 nm (150 and 200 Å). These *D* values coincide with the statistical ones determined by XRD in Figure 4b.

The Figure 7 shows TEM measurements on a Ni particle identified in the sample milled in $O_2$/Ar for 300 min. The Figure 7a shows a SAED ring pattern. The diffracted spots that form rings fit an *F m* $\bar{3}$ *m* structure. The calculated *a* parameter is 3.5 ± 0.5 Å. This value is close to the one reported in Table 1 for this structure. The Figure 7b and 7c show the bright field and dark field images of the particle which SAED pattern is shown in Figure 7a. The bright field image shows agglomerates with sizes larger than 1 μm. The dark field image shows grains with

sizes between 5 and 35 nm. The smaller value is below the detection limits of XRD. Therefore, the Ni structure presents a large distribution of crystallite sizes as shown in Figures 4 b and 7c. Then, both XRD and TEM techniques present complementary results on the size distribution of the crystalline domains of the two structures. The Ni structure has a larger distribution size than the $La_{0.25}Ce_{0.52}Nd_{0.17}Pr_{0.}0_6\ O_2$.

The milling of $La_{0.25}Ce_{0.52}Nd_{0.17}Pr_{0.06}$ - 3Ni in air progresses up to the formation of $La_{0.25}Ce_{0.52}Nd_{0.17}Pr_{0.06}\ O_2$ - 3Ni.

This evolution is shown in the SEM measurements of Figure 8.

This Figure shows the phases distribution after 30 and 300 min of milling, respectively. The Figure 8a shows a micrograph obtained by SEM emissive mode of the mixture of the $La_{0.25}Ce_{0.52}Nd_{0.17}Pr_{0.06}$ and Ni milled 30 min. The image shows a distribution of particles of sizes smaller than 10 μm. The inhomogeneity of the initial milling stage is verified by observing a particle larger than 10 μm located to the right of this image. This type of distribution is typical of this stage [31-32].

The Figure 8b shows the EDS mapping done to the image of Figure 8a. The assigned colors are red for the lanthanides, blue for oxygen and yellow for Ni. The larger particle individualized in Figure 8a is mostly Ni. The color distribution shows a poor homogeneity and the presence of Ni, $La_{0.25}Ce_{0.52}Nd_{0.17}Pr_{0.06}$ and $La_{0.25}Ce_{0.52}Nd_{0.17}Pr_{0.06}O_2$ . The Ni is observed as isolated particles in a continuous matrix of lanthanides.

The milling process affects more the alloy and oxide than the Ni as observed on Figures 2 and 3. The $La_{0.25}Ce_{0.52}Nd_{0.17}Pr_{0.06}O_2$ is not observed by XRD at this stage. It is probably because of the size of the crystalline domains that are under the detection limit of the technique.

The Figure 8 c shows a SEM micrograph in emissive mode of the mixture after 300 min of milling. The Figure 8c shows a more homogeneous surface observed as a large plate. The powder is finer than the powder observed in Figure 8a. This morphology is produced by the cold welding process during milling [16,31-32,34].

The Figure 8 d shows an EDS mapping of the image of Figure 8 c. The color distribution is the same of that of Figure 8b. The phase distribution is more homogeneous than that of Figure 8b. The EDS mapping shows a well interconnected structure between the $La_{0.25}Ce_{0.52}Nd_{0.17}Pr_{0.06}O_2$ (blue/red) and Ni (yellow). The difference between Figures 8a-8b and Fgure 8c-8d is the formation of $La_{0.25}Ce_{0.52}Nd_{0.17}Pr_{0.06}O_2$. The mixture obtained at 300 min, do not show mixed oxides of the form $La_{0.25}Ce_{0.52}Nd_{0.17}Pr_{0.06}O_2$ –Ni-O as observed in the XRD diffractograms of Figures 2 and 3. No intermetallics between Ni and the $La_{0.25}Ce_{0.52}Nd_{0.17}Pr_{0.06}$ are observed and the formation of NiO is not detected as analyzed by TEM.

Since the oxidation of Ni starts at 300 °C, the temperature reaction in the milling jar is below this temperature because NiO is not detected [33]. This is also an advantage that inhibits the diffusion of the components avoiding the formation of intermetallics.

The oxidation of the $La_{0.25}Ce_{0.52}Nd_{0.17}Pr_{0.06}$ inhibits the preferential lamination of the alloy in the chamber and no liquid is needed as a control agent of the process. The milling process produces an intimately mixed metal-oxide composite. The mixture is a fine powder of two constituents with different microstructural parameters as shown in Figures 4b and 4c. The metal is a more relaxed structure than the oxide.

3.2 The second step of the platform: Thermal treatment in air and $H_2$/Ar.

The $La_{0.25}Ce_{0.52}Nd_{0.17}Pr_{0.06}$ $0_2$-3Ni mixture obtained at 300 min is appropriated for use in catalysis and gas capture. The product is a powder that offers an intricate distribution of the components with a more crystalline metal than the oxide. Nevertheless, a further thermal treatment widens the characteristics of the powder and it can be obtained as a mechanically stable pellet extending this platform of treatment. This processing is done in this section.

The Figure 9 a shows the diffractogram of the sample milled 300 min and annealed in air for 12 h at 1400 °C. The diffractogram presents diffraction peaks with a large peak to background ratio. The identified phases are $La_{0.25}Ce_{0.52}Nd_{0.17}Pr_{0.06}O_2$ and NiO . The structural and microstructural properties are characterized by the Rietveld method. A summary of results is shown in Tables 4 and 5. As observed in Table 5, both $La_{0.25}Ce_{0.52}Nd_{0.17}Pr_{0.06}O_2$ and NiO presents large *D* values and low *s* values. The crystallite size of $La_{0.25}Ce_{0.52}Nd_{0.17}Pr_{0.06}O_2$ presented in Table 5 is larger than the *D* value of Figure 4 b. The strain value of $La_{0.25}Ce_{0.52}Nd_{0.17}Pr_{0.06}O_2$ presented in Table 5 is smaller than the *s* value of Figure 4c. The NiO structure also has large values of *D* and small values of *s* as observed in Table 5. NiO and

$La_{0.25}Ce_{0.52}Nd_{0.17}Pr_{0.06}O_2$ develop well-crystallized structures as a result of the treatment in air as deduced from the microstructural values of Table 5.

The Figure 9 b shows the sample of Figure 9 a treated in $Ar/H_2$ for 8 h at 800 °C. The phases present after the reduction in $H_2$/Ar are $La_{0.25}Ce_{0.52}Nd_{0.17}Pr_{0.06}O_2$ , Ni and NiO. The diffractograms are refined by the Rietveld method. The summary of results is presented in Tables 4 and 5. The $La_{0.25}Ce_{0.52}Nd_{0.17}Pr_{0.06}O_2$ of Figure 9 b is less crystalline than $La_{0.25}Ce_{0.52}Nd_{0.17}Pr_{0.06}O_2$ of Figure 9a as observed by comparing the values of *D* and *s* shown in Table 5.

The composite after reduction shows well-crystallized metal and less crystalline oxides.

The Figure 10 shows SEM microimages and EDS measurements done to the pellet of Figure 9 a. The Figure 10a shows a SEM micrograph obtained in emissive mode. The morphology of the particles is smooth with well-defined boundaries and triple joins with angles near 120 °. This morphology is coincident with that of phases grown in equilibrium. The Figure 10 b shows a SEM micrograph obtained in reflective mode of the same zone of Figure 10 a. The bright white zone is assigned to the lanthanides of the $La_{0.25}Ce_{0.52}Nd_{0.17}Pr_{0.06}O_2$ phase. The grey zone is assigned to the Ni of the NiO structure. The black zone is assigned to pores. The image shows the distribution of the two well-developed $F\,m\,\bar{3}\,m$ structures. The Figure 10 c shows an EDS scan-line. The region of interest is indicated in Figures 10a and 10b with a white line. The elements distribution coincides with the Ni and lanthanides presence in the structures assigned in Figure 10b.

The figure 11 shows SEM micrographs and EDS mapping of the sample corresponding to Figure 9b. The Figure 11a shows a SEM micrograph obtained in emissive mode. The sample is the one of Figure 10a treated in $H_2$/Ar. The image shows a porous intricate structure with particles with smooth surfaces. The Figure 11b shows a SEM micrograph obtained in reflective mode of the same zone of Figure 11a. The bright white zone is assigned to lanthanides of the $La_{0.25}Ce_{0.52}Nd_{0.17}Pr_{0.06}O_2$ phase. The grey zone and the black zone are assigned to Ni and pores, respectively. The pellet is more porous than the one observed in Figures 10a and Figure 10 b. This porosity is induced by the reduction of NiO to Ni by $H_2$/Ar. The Figure 11c shows an EDS mapping of the same zone of Figures 10 a and 10 b. The blue color is assigned to Ni. Please, notice the correspondence within the blue zones and the gray ones on Figure 10b. The gray and white colors are assigned to the lanthanides. Notice the similarity between these zones and those of the bright white of Figure 10b. The orange color is assigned to O. These zones are superimposed to those of $La_{0.25}Ce_{0.52}Nd_{0.17}Pr_{0.06.}$ The spatial resolution of the technique is lower than that of the reflective mode. Nevertheless, it is observed that the microstructure is intricate with a connection between the oxide and the metal with a strong adhesion between the metal and the oxide.

The Figure 12 shows the SAED pattern and bright field micrograph of Ni obtained from the same sample observed in Figures 9b and 11. The SAED pattern corresponds to an $F\,m\,\bar{3}\,m$ structure of Ni with a cell parameter of 3.5 ± 0.5 Å. The spots of the SAED pattern are similar to ellipses along to the x axis instead of

circles. This type of shape indicates that the Ni is highly textured. The bright field image of Figure 12 b shows that the Ni consists on particles of sizes close to 600 x 600 nm with straight cuts. The Figure 13 shows the TEM measurements on a $La_{0.25}Ce_{0.52}Nd_{0.17}Pr_{0.06}O_2$ particle obtained from the same sample observed in Figures 9b and 11. The Figure 13 a shows the SAED pattern consistent with the presence of $La_{0.25}Ce_{0.52}Nd_{0.17}Pr_{0.06}O_2$ along [1 $\bar{1}$ 0] zone axis. The white arrows signal a double spot that indicates crystalline domains miss orientation. The Figures 13 b and 13 c show the bright field and dark field of a large particle of $La_{0.25}Ce_{0.52}Nd_{0.17}Pr_{0.06}O_2$. The particle is relatively thick as deduced from the thickness fringes in each micrograph. The figure 13 b has a dashed-white rectangle zoomed out in the inset of this Figure. The inset of Figure 13 b shows the moiré fringes on the particle related to the rectangle. The thickness fringes are also observed in the dark field image. Notice the correspondence between BF and DF in the micrographs of Figures 13 b and 13c.



3.3. A platform for the production of composites

The methods for the fabrication of composites based on $CeO_2$-Ni are numerous and different [7-10]. The most common of them is the wet synthesis followed by thermal treatments [7-10]. The main advantage of these methods is the control of the nanostructure and microstructure with a limited potential of obtain an intricate structure because of the limitations imposed by the starting size of the powders. Less explored than the wet methods, the dry methods offers an alternative and

practical fabrication way. Although using a wet agent, the mechanical milling of $CeO_2$-Ni mixtures is reported [12]. But the control of the final product is limited. In this work, the control of the final powder is done by changing the identity of one of the constituents. The $La_{0.25}Ce_{0.52}Nd_{0.17}Pr_{0.06}$-3Ni mixture is transformed to $La_{0.25}Ce_{0.52}Nd_{0.17}Pr_{0.06}O_2$-3Ni mixture by milling in a controlled $O_2$/Ar gas atmosphere. Since no liquids are added to the process, no extra issues derived from this addition needs to be solved.

As milling progresses, the $La_{0.25}Ce_{0.52}Nd_{0.17}Pr_{0.06}$-3Ni mixture is transformed to a $La_{0.25}Ce_{0.52}Nd_{0.17}Pr_{0.06}O_2$-3Ni mixture. This composite has an intricate structure where the oxides and Ni results in an interconnected structure. The final powder microstructure contains a relatively relaxed metal with a more strained oxide.

The powder can be transformed to a pellet if the composite is thermally treated. The first treatment in air leads to a well- relaxed $La_{0.25}Ce_{0.52}Nd_{0.17}Pr_{0.06}O_2$ -3 NiO mixture. The second treatment in $H_2$/Ar forms a final intricate $La_{0.25}Ce_{0.52}Nd_{0.17}Pr_{0.06}O_2$ -3 Ni composite as a porous pellet with a well related metal and a continuous oxide matrix.

## 4. Conclusions

A platform for the synthesis of metal-oxide composites is obtained in this work. The success of the process is the use of an original metal/alloy starting mixture that promotes the inclusion of the metal in the alloy. The milling in $O_2$/Ar assures that the alloy forms the oxide while still milling. As a result, an intimate mixture is

obtained. Then, two type of metal-oxide composites are obtained from the mechanical milling and thermal annealing process. The first is a porous powder with an intricate metal-oxide mixture. The second is an intricate pellet with an intimate metal-oxide mixture. Both products have the properties needed for use in catalysis and energy conversion.



## 5. Acknowledgements

The authors thank to Servicio de Microscopía Electrónica de Barrido y Difracción de Rayos X of the Centro Atómico Bariloche (CNEA) and to the Grupo de Microscopía Electrónica de Transmisión de la División Física de Metales of the Centro Atómico Bariloche (CNEA). Especial thanks to E. Barragán, M. Corte, A. Geraci and P. Troyón for technical assistance in the use of the TEM and SEM microscopes.

## 6. Funding

This work was partially supported by the Universidad Nacional del Comahue [PI B202-2017-2020]

## 8. References

[1] K.H. Ng, H.A. Rahman, M.R. Somalu, Review: Enhancement of composite anode materials for low-temperature solid oxide fuels, Int. J. Hydrog. Energy, 44 (2019) 30692-30704. https://doi.org/10.1016/j.ijhydene.2018.11.137.

[2] D.B. Pal, R. Chand, S.N. Upadhay, P.K. Mishra, Performance of water gas shift reaction catalyst: A review, Renew. Sust. Energ. Rev. 93 (2018) 549-565. https://doi.org/10.1016/j.rser.2018.05.003.

[3] N.A.K. Aramouni, J.G. Touma, B.A. Tarboush, J. Zeaiter, M.N.Ahmad, Catalyst design for dry reforming of methane: Analysis review, Renew. Sust. Energ. Rev. 82 (2018) 2570-2585. http://dx.doi.org/10.1016/j.rser.2017.09.076

[4] D. Li, Y. Nakagawa, K. Tomishige, Development of Ni-based catalyst for steam reforming of tar derived from biomass pyrolysis. Chin. J. Catal., 33 (2012) 583-594. http:// doi.org/10.1016/S1872-2067(11)60359-8.

[5] I. Sreedhar, B. Agarwal, P. Goyal, S.A. Singh, Recent advances in material and performance aspects of solid oxide fuel cells. J. Electroanal. Chem. 848 (2019) 113315 -113351. https://doi.org/10.1016/j.jelechem.2019.113315.

[6] Y. Zhang, Z. Wang, J.Zhou, J.Liu, K.Cen, Catalytic decomposition of hydrogen iodide over pre-treated Ni/$CeO_2$ catalysts for hydrogen production in the sulfur-iodine cycle, Int. J. Hydrog Energy 34 (2009) 8792-8798. https://doi:10.1016/j.ijhydene.2009.08.058

[7] N. Yahi, S. Menad, I. Rodríguez-Ramos, Dry reforming of methane over Ni/$CeO_2$ catalysts prepared by three different methods. Green Process. Synth. 4 (2015) 479-486. https://doi:10.1515/gps-2015-0061

[8] W. Li, H.Wang, X. Jiang, J.Zhu, Z. Liu, X.Guo, C. Song, A short review of recent advances in $CO_2$ hydrogenation to hydrocarbons over heterogeneous catalysts, RSC Adv.,8 (2018), 7651. https://doi: 10.1039/c7ra13546g.

[9] A.A.A. da Silva, N.Bion, F. Epron, S. Baraka, F.C.Fonseca, R.C. Rabelo-Neto, L.V. Mattos, F.B. Noronha, Effect of the type of ceria dopant on the performance of Ni/$CeO_2$ SOFC anode for ethanol internal reforming, Appl. Catal. B.,206 (2017) 626-641. https://doi.org/10.1016/j.apcatb.2017.01.069..

[10] L.Toscani, M.Genoveva Zimicz, J.R. Casanova, S.A. Larrondo, Ni-Cu/CeO..9Zr0.1O2 bimetallic cermets for electrochemical and catalytic applications, Int. J. Hydrog. Energy, 39 (2014) 8759-8766. http://dx.doi.org/10.1016/j.ijhydene.2013.12.035

[11] S. Phoka, S. Hunpratub, N. Chanlek, S. Sonsupap, S. Maensiri, Synthesis characterization and electrochemical performance of carbon/Ni-doped $CeO_2$

composites, J. Alloy Compd., 750 (2018), 788-797. https://doi.org/10.1016/j.jallcom.2018.04.053.

[12] C. Zhang, S. Li, G.Wu, J.Gong, Synthesis of stable Ni-$CeO_2$ catalysts via ball-milling for ethanol steam reforming, Catal Today, 233 (2014), 53-60 http://dx.doi.org/10.1016/j.cattod.2013.08.013.

[13] R.A.Young (Ed), IUCr Monographs in Crystallography, Oxford University Press, New York, 1993.

[14] S. A. Speakman, An introduction to Rietveld Refinement using PANalytical X´Pert HighScore Plus v3.0e, MIT Center for Materials Science and Engineering (2012).

[15] G.W.H.Höhne, W. Hemminger, H.-J. Flammersheim, Differential Scanning Calorimetry, Second ed., Springer, Berlin-New York, 2003.

[16] C. Suryanarayana, Mechanical alloying and milling, CRC Press - Taylor & Francis, Boca Raton FL, 2004.

[17] R.W.G. Wyckoff, R. W. G. Crystal Structures, Second ed. Insterscience Publishers, New York 1963.

[18] F.H Spedding, A.H Daane, K.W. Herrmann, The crystal structures and lattice parameters of high-purity scandium, yttrium and the rare earth metals Locality: Acta Cryst. 9 (1956) 559-563 https://doi.org/10.1107/S0365110X5600156X

[19] J. Häglund, G. Grimvall, G, A. Fernandez Guillermet, M. Korling, Theory of bonding in transition-metal carbides and nitrides, Phys. Rev. B Condens. Matter, 48 1993 11685-11691. https://doi.org/10.1103/PhysRevB.48.11685

[20]. A. Nakaue, Studies on the pressure-temperature phase diagram of Nd, Sm, Gd and Dy, J Less Common Met, 60 (1978) 47-58. https://doi.org/10.1016/0022-5088(78)90088-7

[21] K. A. Gschneidner Jr, Systematics of the Intra-rare-earth binary alloy systems, J.Less Common Met, 114 (1985) 29-42. https://doi.org/10.1016/0022-5088(85)90387-X.

[22] G. Wulfsberg , Inorganic Chemistry, University Science Books, Sausalito CA, 2000.

[23] Z. Du, D. Wang, W. Zhang, Thermodynamic assessment of the La-Ni system, J. Alloy Compd., 264 (1998), 209-213. https://doi.org/10.1016/S0925-8388(97)00269-7

[24] W. Xiong, Y.Du, X.Lu, J.C. Schuster, H. Chen, Reassessment of the Ce-Ni binary system supported by key experiments and ab initio calculations, Intermetallics 15 (2007), 1401-1408. https:// doi:10.1016/j.intermet.2007.04.004

[25] Z. Rahou, K. Mahdouk, D. Moustain, S. Otmani, S. Kardellass, A. Iddaoudi, N. Selhaoui, Thermodynamic reassessment of Ni-Pr binary system, J. Alloy Compd. 620 (2015), 204-209. http://dx.doi.org/10.1016/j.jallcom.2014.09.116

[26] A. Hussain, M-A. Van Ende, J.Kim, I-H. Jung, Critical thermodynamic evaluation and optimization of the Co-Nd, Cu-Nd and Nd-Ni systems, Calphad 41 (2013) 26-41 http://dx.doi.org/10.1016/j.calphad.2012.12.003.

[27] C.K. Gupta, N. Krishnamurthy, Extractive Metallurgy of Rare Earths, CRC Press, Boca Raton Fl, 2005.

[28] A. Leineweber, H. Jacobs, S. Hull, Orderign of Nitrogen in Nickel Nitride $Ni_3N$ determined by Neutron Diffraction, Inorg. Chem., 40 (2001) 5818-5822. https://doi.org/10.1021/ic0104860.

[29] E.H.P. Cordfunke, R.J.M. Konings, The enthalpies of formation of lanthanide compounds III. $Ln_2O_3$ (cr), Thermochim. Acta, 375 (2001) 65-79. https://doi.org/10.1016/S0040-6031(01)00510-X.

[30] S.A. Gramsch, L.R. Morss, Standard molar enthalpies of formation of $PrO_2$ , and SrPrO3: the unusual thermodynamic stability of $APrO_3$ (A=Sr,Ba), J.Chem Thermodynamics, 27 (1995) 551-560 https://doi:10.1006/jcht.1995.0056

[31] L. Lu, M.O.Lai, Mechanical alloying, Springer, Boston, 1988.

[32] S. Obregón, J.J. Andrade-Gamboa, M.R. Esquivel, Synthesis of Al-containing $MmNi_5$ by mechanical alloying: milling stages, structure parameters and thermal annealing, Int. J. Hydrog. Energy, 37 (2012) 14972-1977.

[33] S.Cabanas-Polo, R. Bermejo, B. Ferrari, A.J. Sanchez-Herencia, Ni-Nio composites obtained by controlled oxidation of green compacts, Corros. Sci. 55 (2012) 172-179. https;// doi:10.1016/j.corsci.2011.10.016.

[34] N.M.Cerón-Hurtado, M.R. Esquivel, Stages of mechanical alloying during the synthesis of Sn-containing $AB_5$-based intermetallics, Int.J. Hydrog. Energy, 35 (2010) 6057-6062. https://doi.org/10.1016/j.ijhydene.2009.12.072.

Captions of Figures

Figure 1. Diffractograms of the starting components. a) The $La_{0.25}Ce_{0.52}Nd_{0.17}Pr_{0.06}$ alloy. The letters y and z stand for the cubic (*F m* $\bar{3}$ *m )* and hexagonal (*P*6/$_3$*mmc)* structures, respectively. b) Ni. The letter x stands for the Ni (*F m* $\bar{3}$ *m)* structure.

Figure 2. Diffractograms of the $La_{0.25}Ce_{0.52}Nd_{0.17}Pr_{0.06}$ – 3Ni mixture obtained at different milling times. a) 30 min. b) 60 min. c) 90 min. d) 120 min. e) 180 min. f) 300 min. The letters y, z stand for the *F m* $\bar{3}$ *m* and *P*6$_3$/*mmc* polymorphs of the $La_{0.25}Ce_{0.52}Nd_{0.17}Pr_{0.06}$ alloy. The letter x stands for the Ni structure. The letter u stands for the $La_{0.25}Ce_{0.52}Nd_{0.17}Pr_{0.06}O_2$ (*F m* $\bar{3}$ *m* ) structure. A detail of the 2θ range from 25 to 35 is shown in Figure 3.

Figure 3. Detail of the diffractograms of the $La_{0.25}Ce_{0.52}Nd_{0.17}Pr_{0.06}$ – 3Ni mixture obtained at different milling times. a) 30 min. b) 60 min. c) 90 min. d) 120 min. e) 180 min. f) 300 min. The letters y, z stand for the *F m* $\bar{3}$ *m* and *P*6$_3$/*mmc* polymorphs of the $La_{0.25}Ce_{0.52}Nd_{0.17}Pr_{0.06}$ alloy. The letter x stands for the Ni structure. The letter u stands for the $La_{0.25}Ce_{0.52}Nd_{0.17}Pr_{0.06}O_2$ (*F m* $\bar{3}$ *m* ) structure.

Figure 4. The evolution of the different parameters quantifying the milling process as a function of time. a) Mass percent of the crystalline phases. b) Crystallite size (*D*) c) Strain (*s*).

Figure 5. The thermal evolution of the $La_{0.25}Ce_{0.52}Nd_{0.17}Pr_{0.06}$ alloy in air. The heat of formation is obtained by using eq. (1). The stoichiometry of the reaction is defined by eq. (2).

Figure 6. TEM techniques applied to a characteristic particle of $La_{0.25}Ce_{0.52}Nd_{0.17}Pr_{0.06}O_2$ in the sample milled 300 min in $O_2$/Ar. a) SAED ring pattern. b) Bright field (BF) image. c) Dark field (DF) image.

Figure 7. TEM techniques applied to a characteristic particle of Ni in the sample milled 300 min in $O_2$/Ar. a) SAED ring pattern. b) Bright field (BF) image. c) Dark field (DF) image.

Figure 8. SEM measurements on samples milled 30 min and 300 min. a) SEM micrograph obtained in emissive mode of the sample milled 30 min. b) EDS mapping of the sample of micrograph 8a. c) SEM micrograph obtained in emissive mode of the sample 300 min. d) EDS mapping of the sample of micrograph 8c. Color assignment is blue for O, red for the lanthanides and yellow for Ni in both Figures 8b and 8d.

Figure 9. Diffractograms of the samples milled 300 min and thermally treated. a) In air for 12 h at 1400 °C. b) In $H_2$/Ar for 8 h at 800 °C. The letters x, w, u stand for Ni, NiO and $La_{0.25}Ce_{0.52}Nd_{0.17}Pr_{0.06}O_2$, respectively.

Figure 10. SEM measurements done to the sample treated at 1400 °C in air . a) SEM micrograph obtained in emissive mode. b) SEM micrograph obtained in reflective mode. c) Line-scan of the sample. The line-scan is done to the zone indicated with a white line in micrographs of Figure 10a and Figure 10b.

Figure 11. SEM measurements done to the sample treated in $H_2$/Ar. a) SEM micrograph obtained in emissive mode. b) SEM micrograph obtained in reflective mode. c) EDS mapping. The blue color is assigned to Ni, the white – gray color to the lanthanides and the orange color to oxygen.

Figure 12. a) TEM selected area diffraction (SAED) ring pattern of Ni after heat treatments. b) TEM bright field image of the particle which SAED pattern is presented in Fig. 12.a.

Figure 13. a) TEM selected area diffraction (SAED) pattern of a $La_{0.25}Ce_{0.52}Nd_{0.17}Pr_{0.06}O_2$ particle. The zone axis is $[1\ \bar{1}\ 0]$. The white arrows indicate a domain miss orientation. b) TEM bright field image. The white-dash rectangle shows moiré fringes on the particle. c) TEM dark field image. Notice the thickness fringes of the particle in the BF and DF.

Tables and captions of tables

Table 1. Structural properties of the $La_{0.25}Ce_{0.52}Nd_{0.17}Pr_{0.06}$ polymorphs and Ni obtained from the Rietveld refinement. The lanthanide atoms are randomly distributed in the $Fm\bar{3}m$ and the $P6_3/mmc$ structure of the $La_{0.25}Ce_{0.52}Nd_{0.17}Pr_{0.06}$ according to the nominal composition. SG and FU stand for space group and formula unit, respectively. M is the multiplicity of the Wyckoff (Wy) position. GOF stands for the goodness of the fit.

| Figure | Structure SG / FU | Cell parameters (Å), (°) | | Atomic positions / coordinates M / Wy | (x,y,z) | Mass % ± 2 | GOF |
|---|---|---|---|---|---|---|---|
| 1.a | $La_{0.25}Ce_{0.52}Nd_{0.17}Pr_{0.06}$ $P6_3/mmc$ 4 | $a$ , $b$ | 3.59625(9) | 2a | 0,0,0 | 5 | 2 |
| | | $c$ | 12,9838(4) | 2c | +1/3, -1/3, +1/4 | | |
| | | $\alpha, \beta, \gamma$ | 90,90,120 | | | | |
| | $La_{0.25}Ce_{0.52}Nd_{0.17}Pr_{0.06}$ $Fm\bar{3}m$ 4 | a , b, c | 5.21652(5) | 4a | 0,0,0 | 95 | |
| | | $\alpha, \beta, \gamma$ | 90,90,90 | | | | |
| 1.b | *Ni* $Fm\bar{3}m$ *4* | $a$ , $b$,$c$ | 3.52833(6) | 4a | 0,0,0 | 100 | 1.50 |
| | | $\alpha, \beta, \gamma$ | 90,90,90 | | | | |

Table 2.

A comparison of the cell parameters of the polymorphs of $La_{0.25}Ce_{0.52}Nd_{0.17}Pr_{0.06}$ and those of the pure rare earth metals La, Ce, Nd and Pr.

| Compound | SG | Cell parameters | | | Ref |
|---|---|---|---|---|---|
| | | *a*, *b* (Å) | *c* (Å) | *V* (Å$^3$) | |
| $La_{0.25}Ce_{0.52}Nd_{0.17}Pr_{0.06}$ | *P*6$_3$/*mmc* | 3.59(6) | 12,98(3) | 144.8(7) | This work |
| La | | 3.770 | 12.159 | 149.62 | 17 |
| Ce | | 3.65 | 11.91 | 137.484 | 17 |
| Nd | | 3.6579 | 11.7992 | 136.725 | 18 |
| Pr | | 3.6725 | 11.8354 | 138.241 | 18 |
| $La_{0.25}Ce_{0.52}Nd_{0.17}Pr_{0.06}$ | *F m* $\bar{3}$ *m* | 5.216(2) | | 141.9(0) | This work |
| La | | 5.32 | | 150.59 | 19 |
| Ce | | 5.1612 | | 137.484 | 18 |
| Nd | | 4.917 | | 118.878 | 20 |
| Pr | | 5.161 | | 137.468 | 17 |

Table 3. The microstructural parameters for the selected peaks of the structures of Figure 1. SG and GOF stand for the space group and the goodness of the fit, respectively.

| Compound<br>SG | hkl | 2(θ) | *D* ± 10<br>(Å) | *s* ± 0.05<br>(%) | GOF |
|---|---|---|---|---|---|
| $La_{0.25}Ce_{0.52}Nd_{0.17}Pr_{0.06}$ | {100} | 28.50 | 40 | 3 | 2 |
| *P*6$_3$/*mmc* | {101} | 29.33 | 40 | 3 | |
| $La_{0.25}Ce_{0.52}Nd_{0.17}Pr_{0.06}$ | {111} | 29.50 | 40 | 3.60 | |
| *F m* $\bar{3}$ *m* | {200} | 34.21 | 45 | 2.80 | |

| | | | | | | |
|---|---|---|---|---|---|---|
| | Ni | {111} | 44.52 | 1300 | 0.15 | 1.50 |
| | $F\,m\,\bar{3}\,m$ | {200} | 51.86 | 880 | 0.10 | |

Table 4. The structural parameters obtained by Rietveld refinement of the structures of diffractograms of Figure 9. The lanthanides are randomly distributed within the $La_{0.25}Ce_{0.52}Nd_{0.17}Pr_{0.06}O_2$ structure. The occupancy factor of the lanthanides is distributed according to the nominal composition.

| Figure | Structure SG / FU | Cell parameters (Å), (°) | | Element /Multiplicity /Wyckoff positions / coordinates | | | Mass % ± 2 | GOF |
|---|---|---|---|---|---|---|---|---|
| | | | | Element | M/Wy | (x,y,z) | | |
| 9.a | $La_{0.25}Ce_{0.52}Nd_{0.17}Pr_{0.06}O_2$ | *a , b,c* | 5.5300 (5) | La,Ce,Nd,Pr/ | 4a | (0,0,0) | 30 | 1.90 |
| | $F\,m\,\bar{3}\,m$ | | | | | | | |
| | 4 | *α, β, γ* | 90 | O | 8c | ($^1/_4$,$^1/_4$,$^1/_4$) | | |
| | NiO | *a , b, c* | 5.2165 2(5) | Ni | 4b | 0,0,0 | 70 | |
| | $F\,m\,\bar{3}\,m$ | | | | | | | |
| | 4 | *α, β, γ* | 90 | O | 4a | ($^1/_2$,$^1/_2$, $^1/_2$) | | |
| 9.b | $La_{0.25}Ce_{0.52}Nd_{0.17}Pr_{0.06}O_2$ | *a,b,c* | 5.5299 (5) | La,Ce,Nd,Pr | 4a | (0,0,0) | 30 | 1.65 |
| | $F\,m\,\bar{3}\,m$ | | | | | | | |
| | 4 | *α, β, γ* | 90 | O | 8c | ($^1/_4$,$^1/_4$,$^1/_4$) | | |
| | NiO | *a,b,c* | 4.1743 4(0) | Ni | 4b | 0,0,0 | 12 | |
| | $F\,m\,\bar{3}\,m$ | | | | | | | |
| | 4 | *α, β, γ* | 90 | O | 4a | ($^1/_2$,$^1/_2$, $^1/_2$) | | |
| | Ni | *a,b,c* | 3.5221 (7) | Ni | 4a | (0,0,0) | 54 | |

| | | | | | |
|---|---|---|---|---|---|
| | $Fm\bar{3}m$ | $\alpha, \beta, \gamma$ | 90 | | |
| | 4 | | | | |

Table 5. The microstructural parameters for the selected peaks of the structures of Figure 9. SG and GOF stand for the space group and the goodness of the fit, respectively.

| Figure | Compound<br>SG | hkl | 2(θ) | $D \pm 10$<br>(Å) | $s \pm 0.05$<br>(%) | GOF |
|---|---|---|---|---|---|---|
| 9a | $La_{0.25}Ce_{0.52}Nd_{0.17}Pr_{0.06}O_2$ | {111} | 27.89 | >2000 | 0.05 | 1.90 |
| | $Fm\bar{3}m$ | {200} | 32.33 | >2000 | 0.05 | |
| | NiO | {111} | 37.14 | >2000 | <0.01 | |
| | $Fm\bar{3}m$ | {200} | 43.17 | >2000 | <0.01 | |
| 9b | $La_{0.25}Ce_{0.52}Nd_{0.17}Pr_{0.06}O_2$ | {111} | 27.77 | 190 | 0.85 | 1.65 |
| | $Fm\bar{3}m$ | {200} | 32.20 | 175 | 0.79 | |
| | NiO | {111} | 37.09 | 345 | 0.65 | |
| | $Fm\bar{3}m$ | {200} | 43.12 | 245 | 0.42 | |
| | Ni | {111} | 44.33 | >2000 | <0.01 | |
| | $Fm\bar{3}m$ | {200} | 51.68 | >2000 | <0.01 | |

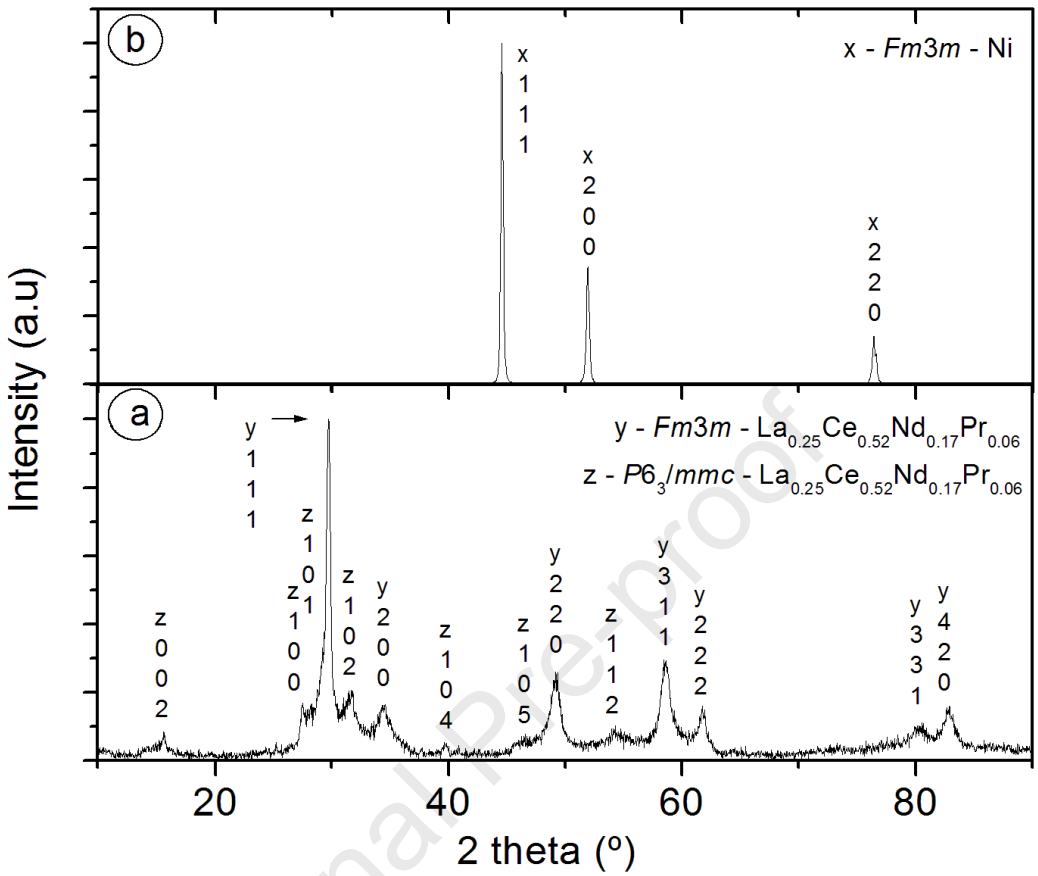

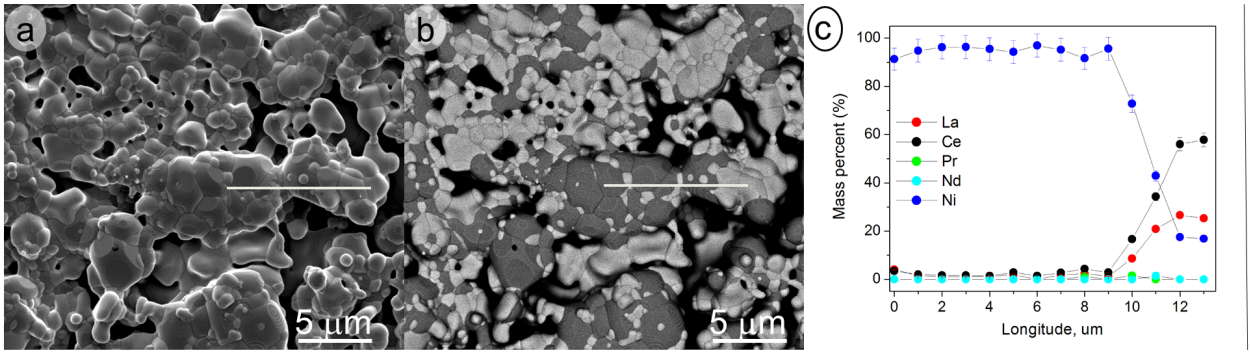

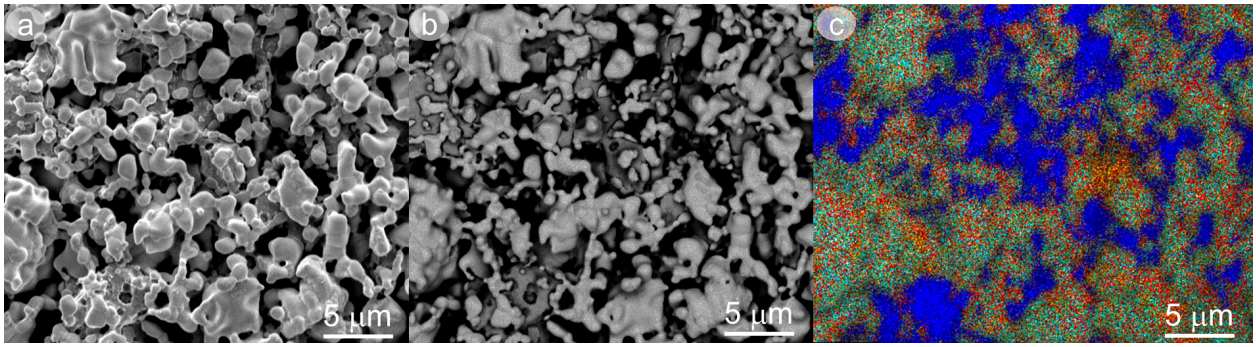

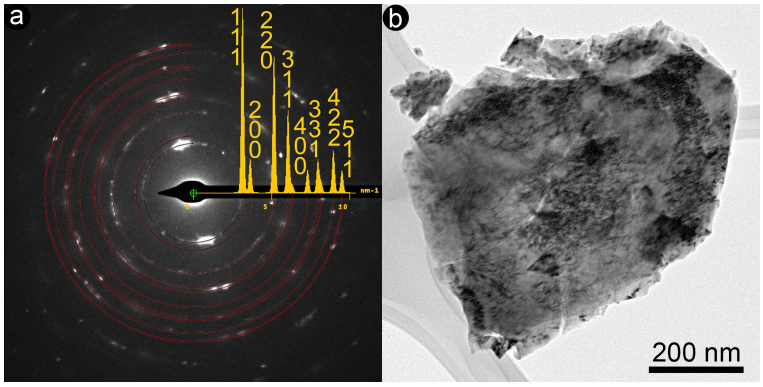

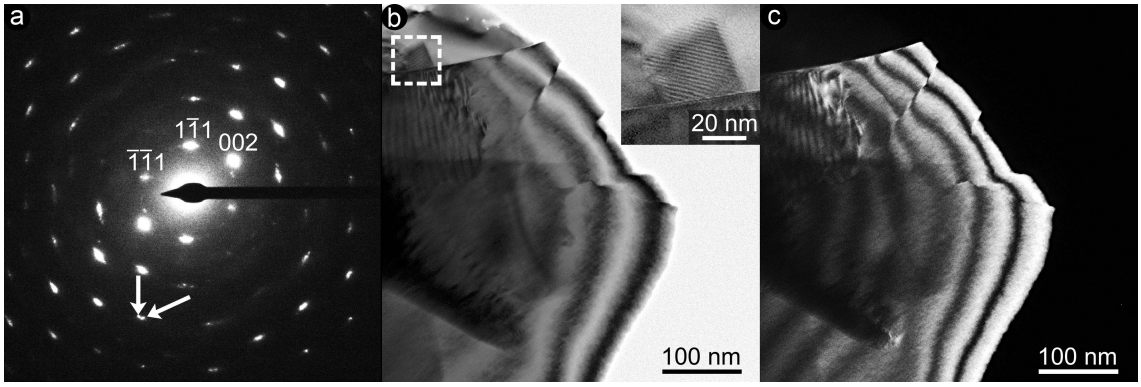

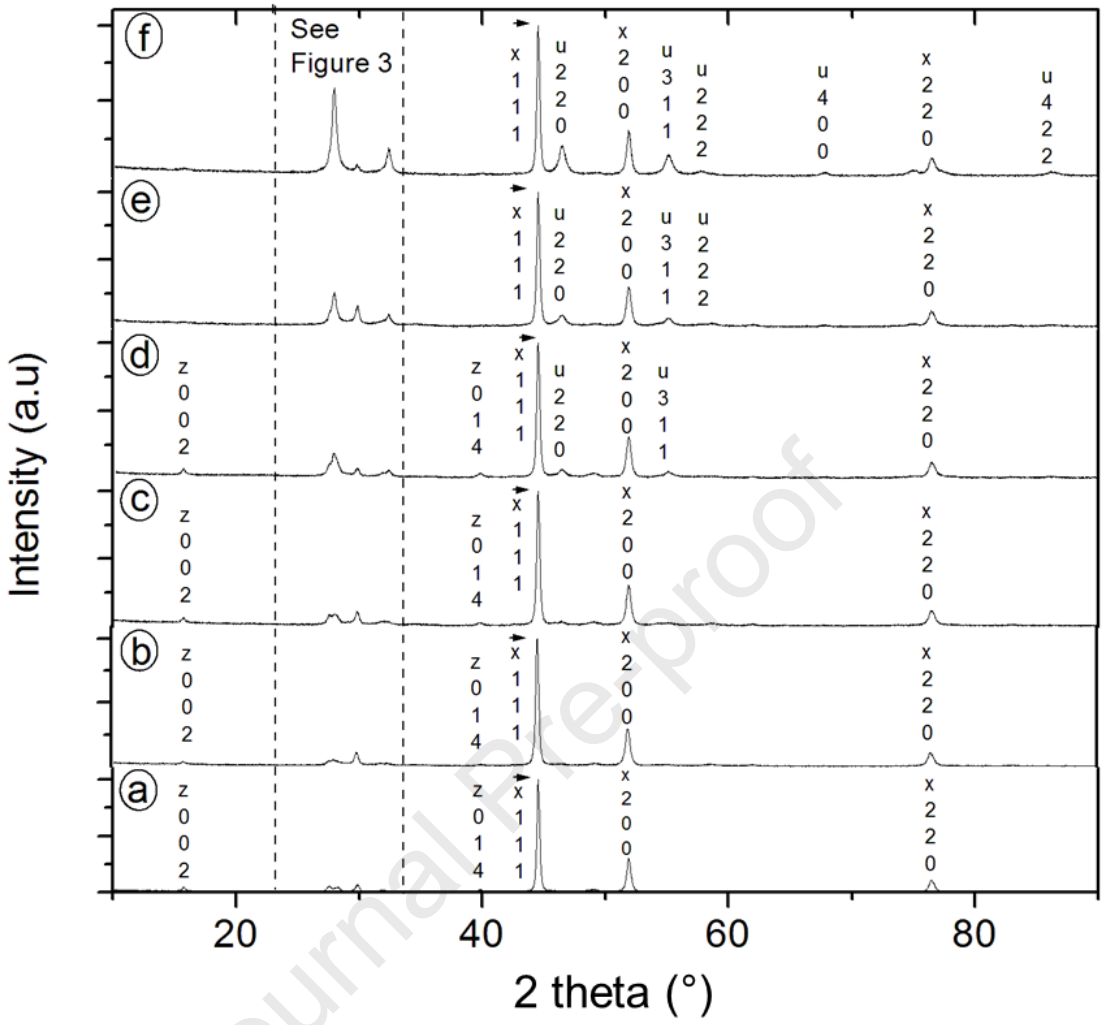

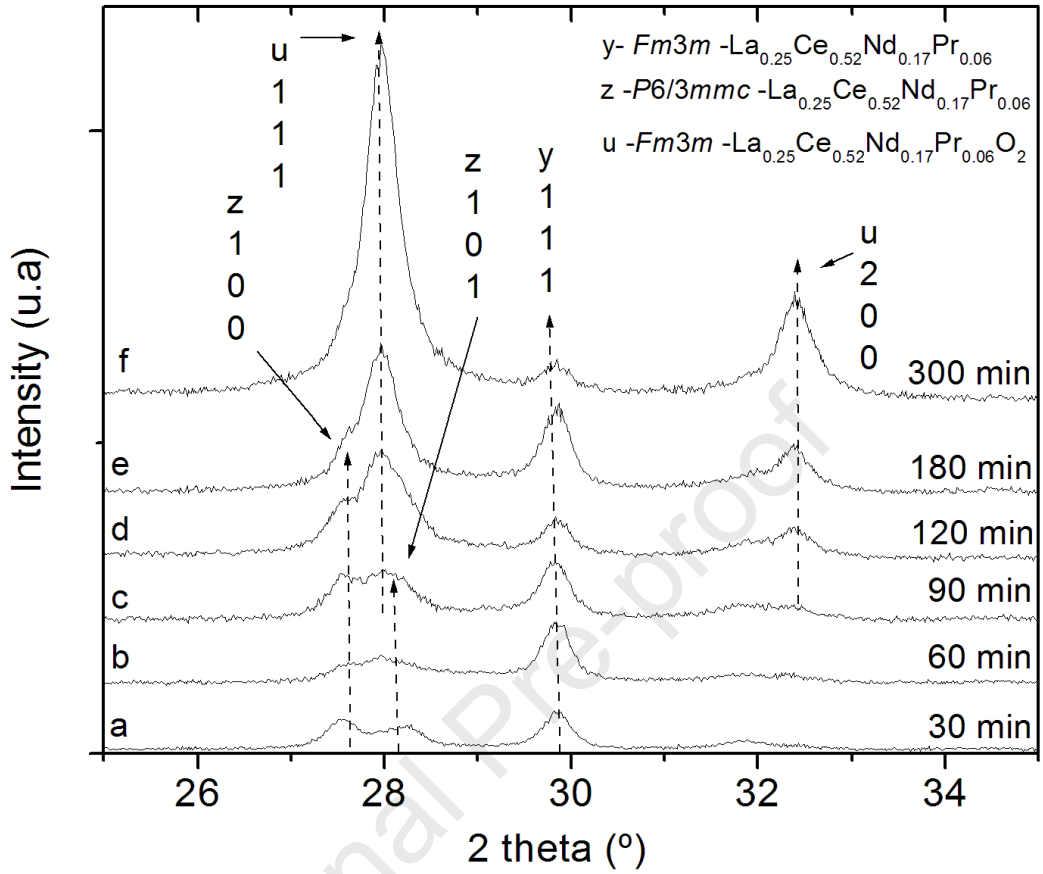

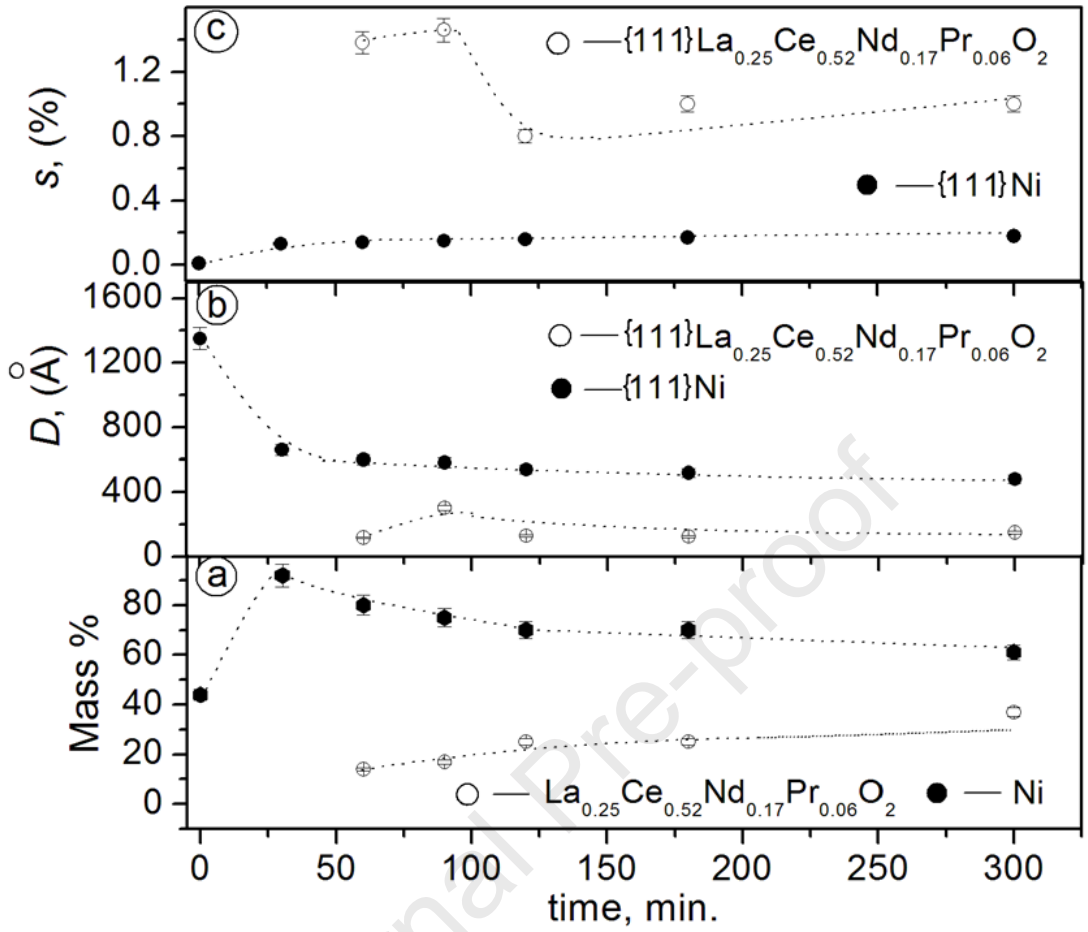

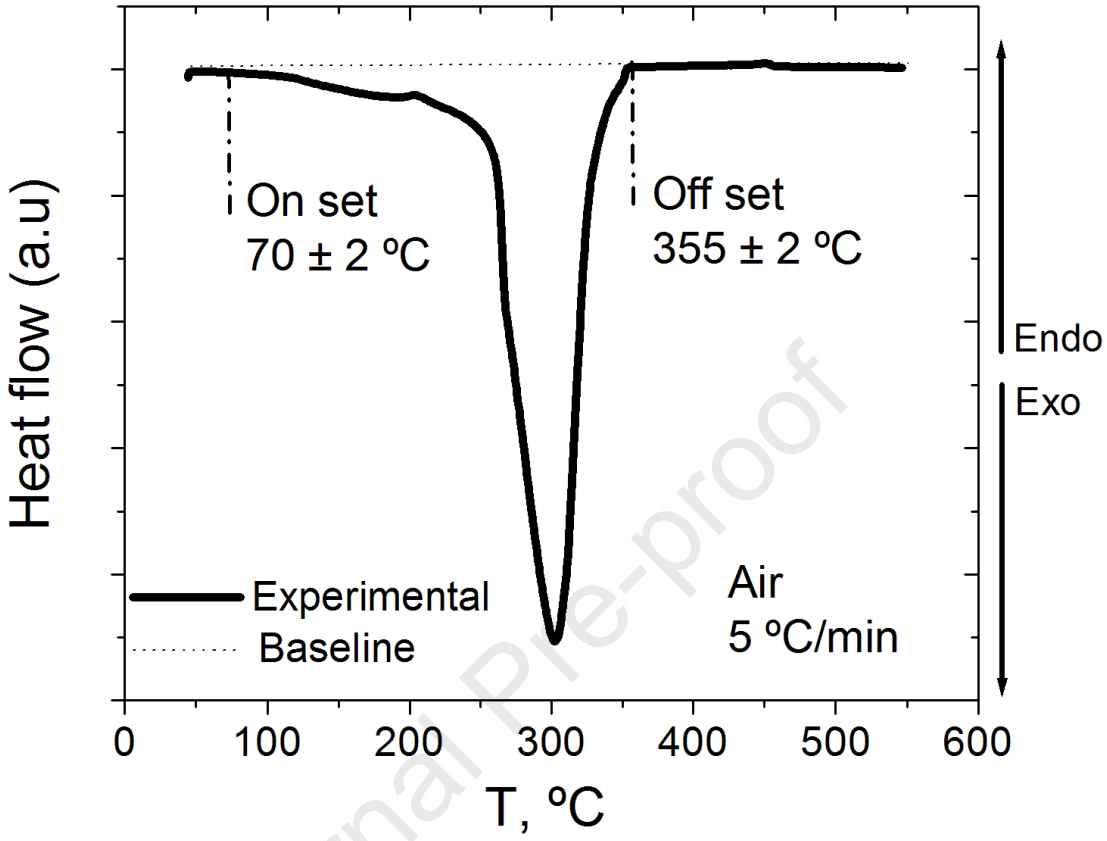

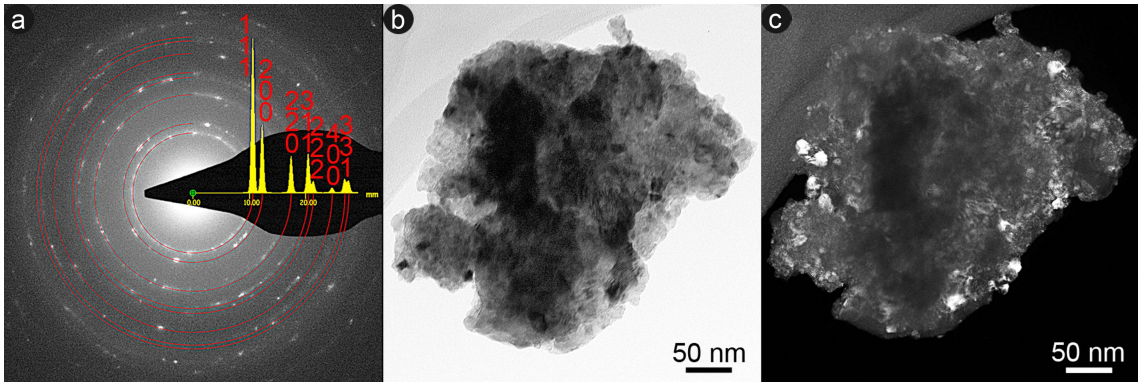

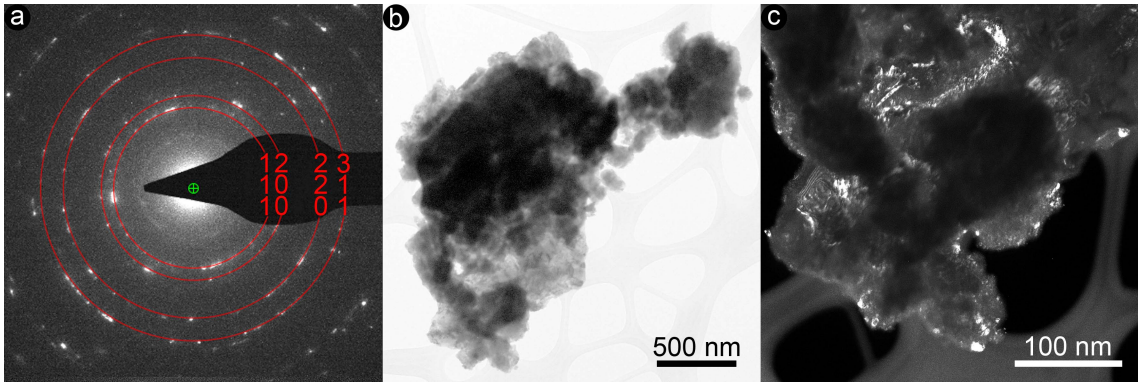

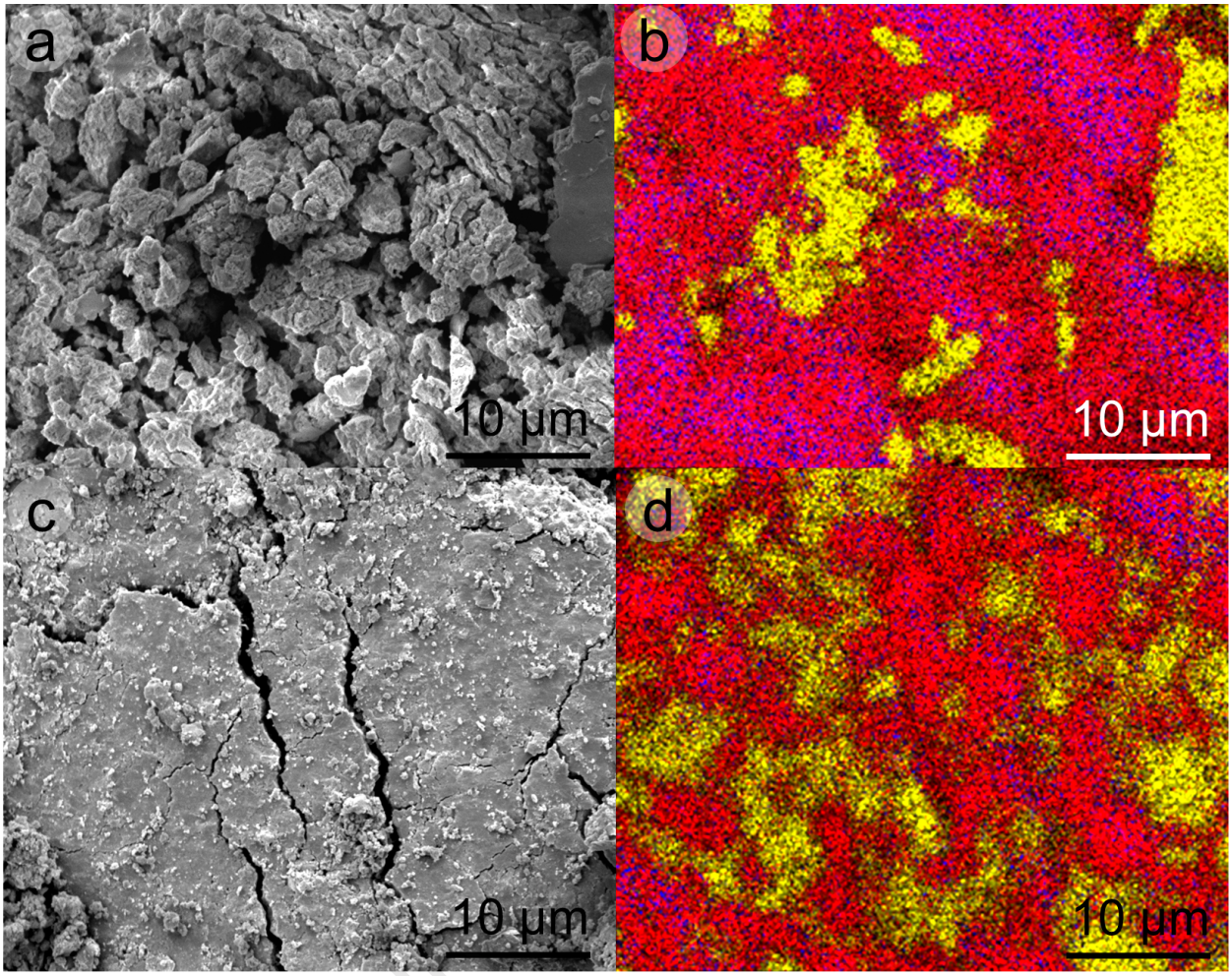

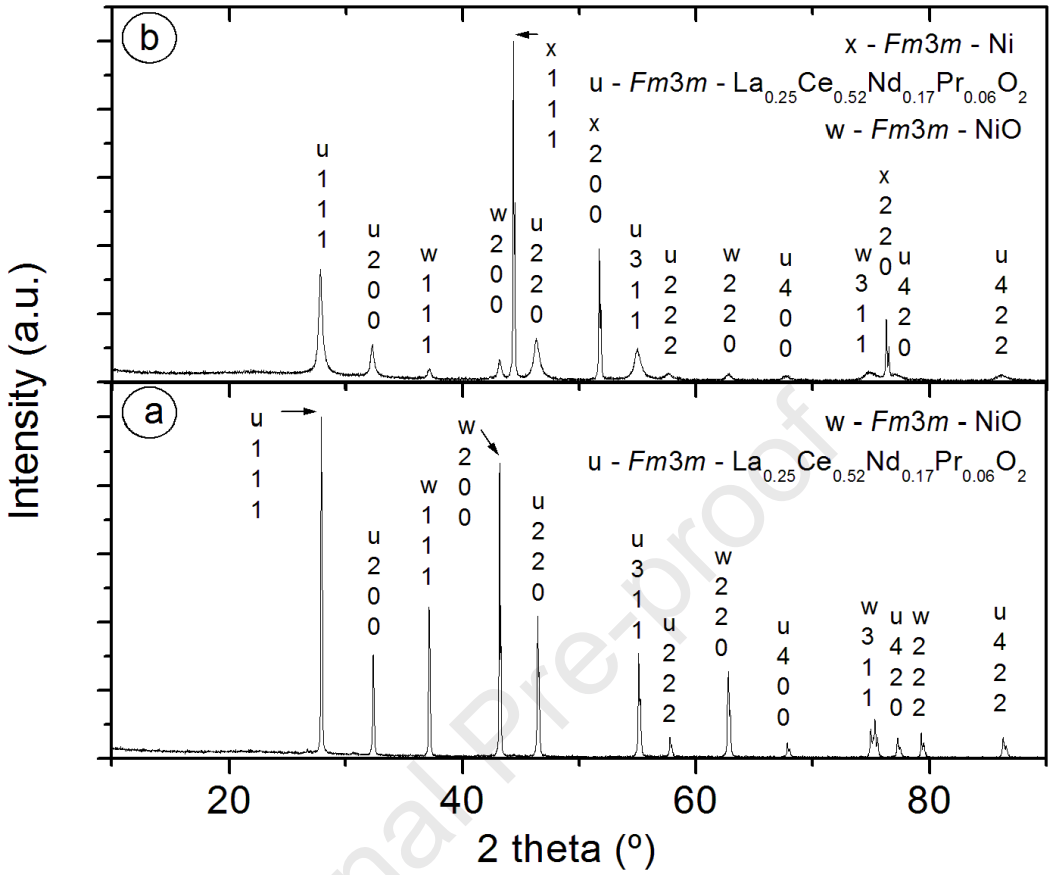

**Declaration of interests**

☒ The authors declare that they have no known competing financial interests or personal relationships that could have appeared to influence the work reported in this paper.

☒The authors declare the following financial interests/personal relationships which may be considered as potential competing interests:

NONE.